Source model for the M_w 6.7, 23 October 2002, Nenana Mountain Earthquake (Alaska) from InSAR

Tim J. Wright,[1] Zhong Lu,[2] and Chuck Wicks[3]

Received 20 June 2003; revised 7 August 2003; accepted 14 August 2003; published 30 September 2003.

[1] The 23 October 2002 Nenana Mountain Earthquake ($M_w \sim 6.7$) occurred on the Denali Fault (Alaska), to the west of the $M_w \sim 7.9$ Denali Earthquake that ruptured the same fault 11 days later. We used 6 interferograms, constructed using radar images from the Canadian Radarsat-1 and European ERS-2 satellites, to determine the coseismic surface deformation and a source model. Data were acquired on ascending and descending satellite passes, with incidence angles between 23 and 45 degrees, and time intervals of 72 days or less. Modeling the event as dislocations in an elastic half space suggests that there was nearly 0.9 m of right-lateral strike-slip motion at depth, on a near-vertical fault, and that the maximum slip in the top 4 km of crust was less than 0.2 m. The Nenana Mountain Earthquake increased the Coulomb stress at the future hypocenter of the 3 November 2002, Denali Earthquake by 30–60 kPa. *INDEX TERMS:* 1242 Geodesy and Gravity: Seismic deformations (7205); 6969 Radio Science: Remote sensing; 1243 Geodesy and Gravity: Space geodetic surveys; 7215 Seismology: Earthquake parameters. **Citation:** Wright, T. J., Z. Lu, and C. Wicks, Source model for the M_w 6.7, 23 October 2002, Nenana Mountain Earthquake (Alaska) from InSAR, *Geophys. Res. Lett.*, *30*(18), 1974, doi:10.1029/2003GL018014, 2003.

1. Introduction

[2] The Nenana Mountain Earthquake created a linear aftershock zone some 40 km long, centred on the Denali Fault in interior Alaska, 140 km south of Fairbanks (Figure 1). No evidence of surface rupture was found [P. Haeussler, K. Sieh, personal communication, 2003]. Teleseismic focal mechanisms suggest the earthquake ruptured a vertical fault at shallow depth (Figure 1). It occurred 11 days prior to, and immediately west of, the M_w 7.9, 3 November, Denali Earthquake–one of the largest earthquakes to rupture continental crust in the instrumental period [*Eberhart-Phillips-et al.*, 2003]. Obtaining an accurate slip model for the Nenana Mountain Earthquake is therefore of great importance for understanding the relationship between these two events.

2. InSAR Data

[3] Since the launch of ERS-1 in 1991, Synthetic Aperture Radar Interferometry (InSAR) has become a widely used technique for mapping deformation of the earth's surface caused by earthquakes [e.g., *Wright*, 2002]. We produced one 35-day interferogram using data from ERS-2 and 5 interferograms using data from the Canadian Radarsat-1 satellite (Table 1). Like the SAR on the ERS satellites, the Radarsat-1 SAR operates at C-band wavelengths (56.7 mm). Its orbital repeat time of 24 days is 11 days shorter than that of ERS, and it also has the advantage of having multiple beam modes, with different incidence angles. This enables multiple acquisitions over the same area from different satellite passes – we formed interferograms using Radarsat-1 standard beam mode images acquired on 4 dates between 23 October and 3 November 2002, with four different viewing geometries. All interferograms had time intervals between 24 and 72 days, and perpendicular baselines, $B_\perp$, less than 130 m (Table 1). Unfortunately, changes in Radarsat-1's beam mode resulted in interferograms ifm1 and ifm5 capturing only the southern half of the deformation field.

[4] Interferograms were processed using the 2-pass method with a 60 m Digital Elevation Model from the USGS to remove residual topographic fringes [*Massonnet and Feigl*, 1998]. The DEM has a nominal rms vertical error of ~15 m, which translates to no more than 3 mm of rms range change error. The interferograms were cleaned using a power spectrum filter [*Goldstein and Werner*, 1998] and unwrapped. Because the poor accuracy of the orbital models available for Radarsat-1, the nominal baseline required refinement. This was done by finding the baseline that minimised the square misfit between the interferogram and a simulation calculated from the DEM. Nevertheless, some residual quadratic phase ramps remained in the interferograms. To deal with these, a best-fit quadratic surface was determined and subtracted from each interferogram, after predictions from a first-pass earthquake model had been removed.

[5] The deformation resulting from the Nenana Mountain Earthquake is clear in every interferogram (Figure 2a), but the different viewing geometries result in very different interferograms. This is most noticeable in the difference between the ascending interferograms ifm1 and ifm5 and those acquired on descending passes (ifm2–4): the ascending interferograms show range decreases south of the Denali fault, whereas range increases are evident in the descending interferograms. This is consistent with predominantly horizontal motion, caused by right-lateral slip on the Denali Fault. Several interferograms contained small discontinuities at, or near to, the mapped trace of the Denali Fault. Incoherence in these areas meant that the magnitude of any offsets could not be determined reliably.

3. Modeling

[6] We used the InSAR data to solve for a simple uniform-slip model and a more complex, distributed-slip

[1]COMET, Department of Earth Sciences, Oxford University, UK.
[2]USGS, EROS Data Center, SAIC, South Dakota, USA.
[3]USGS, Menlo Park, California, USA.

0094-8276/03/2003GL018014

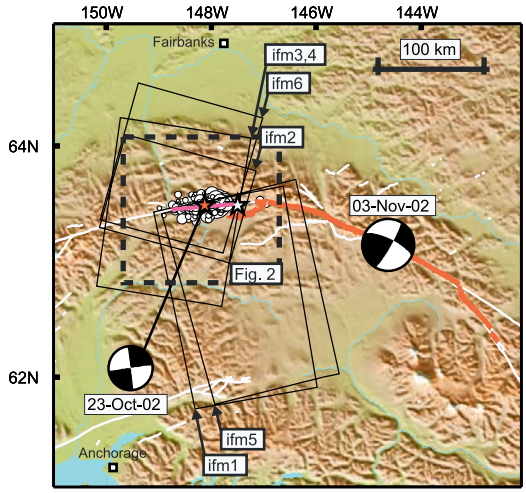

Figure 1. Topographic and tectonic map of the region surrounding the 2002 Denali Fault earthquakes. White lines show previously mapped faults and the red line is the mapped rupture of the 3 November 2002 earthquake. Focal mechanisms are from Harvard CMT; white circles show earthquakes occurring between 23 and 31 October 2002, and the red and white stars indicate the epicentres of the 23 October and 3 November mainshocks respectively (Alaska Earthquake Information Center). Black lines delimit the extents of the InSAR data used for this study, and the magenta line is the surface trace of the distributed-slip model fault.

model. To prepare the data for inversion, we subsampled the interferograms using the Quadtree algorithm [e.g., *Jónsson et al.*, 2002], using a variance threshold and maximum block size equal to the variance and length scale of each interferogram's noise (Table 1), and a minimum block size of 640 m. This reduced the number of phase samples in each interferogram to between 270 and 650. Because of the high degree of spatial correlation of the InSAR data [e.g., *Hanssen*, 2001], little relevant information is lost in this process.

3.1. Uniform-Slip Model

[7] Initially we modelled the earthquake as equivalent to a single rectangular dislocation in an elastic half space [*Okada*, 1985]. Nine fault parameters (Table 2) were determined in the inversion procedure, which minimizes the square misfit between the observed and predicted phase changes using a non-linear, downhill simplex algorithm with Monte Carlo restarts to avoid local minima [e.g., *Wright et al.*, 1999]. Predicted phase changes were determined by projecting the 3D displacement vector into the satellite line of sight, calculated independently for each observation location. The data were weighted equally. We also solved for best-fit planes and linear offsets for each interferogram, although these were negligible because we had already removed best-fit quadratic phase surfaces.

[8] The orientation of the fault plane, and geodetic moment, are in good agreement with estimates from seismology. Slip could not be determined independently from fault width – very narrow fault planes, with high slip, centred at a depth of ~10 km have similar misfit to wider faults with less slip. The product of slip and width (potency) was approximately constant. We chose to fix the slip at 1 m, consistent with slip-length scaling laws [e.g., *Pegler and Das*, 1996], which resulted in a depth range of 5.2 to 20.6 km. The surface projection of the fault plane is coincident with the mapped Denali Fault, although it is shorter than the aftershock zone.

Table 1. Interferograms Constructed for This Study

	date 1	date 2	θ^a	α^b	$B_\perp{}^c$	σ^d	l^e
ifm1	7-Sep-02	25-Oct-02	39.2	−10.8	−45	5.7	8.8
ifm2	2-Oct-02	26-Oct-02	23.8	−164.4	−69	8.5	5.6
ifm3	16-Aug-02	27-Oct-02	44.4	−170.9	−16	7.3	11.5
ifm4	3-Oct-02	27-Oct-02	44.4	−170.9	−127	10.8	11.2
ifm5	5-Oct-02	29-Oct-02	27.8	−14.1	−10	9.9	12.0
ifm6[f]	24-Sep-02	29-Oct-02	23.3	−164.4	56	6.5	4.4

[a]Incidence angle at scene center.
[b]Satellite Azimuth (angle between the satellite ground track and local north).
[c]Perpendicular baseline (metres).
[d]Standard deviation of the interferogram's noise (mm).
[e]e-folding length scale of the interferogram's 1D covariance function (km), calculated using data from the whole interferogram [*Hanssen*, 2001], with data masked out within 25 km of the projected fault rupture.
[f]Data from ERS-2.

[9] Parameter errors were determined using Monte Carlo simulation of correlated noise (Wright et al., manuscript in preparation, 2003). In this method, multiple sets of correlated noise that have the same covariance function as observed in the data are simulated. 100 such data sets are added to the observed phase changes; parameter errors are determined from the distribution of the best-fit solutions to each of these noisy data sets. In addition, tradeoffs between parameters can be investigated. We found that errors and tradeoffs were greatly reduced by using all the available data, compared to inversions in which only a single ascending or descending interferogram were used (Auxiliary Figure 1[1]). For example, fault rake has a 1σ-error of 8.5° when using only ifm1 (ascending), 4.5° using ifm3 (descending) only, but only 1.3° using all 6 interferograms. Synthetic interferograms and residuals for this model were calculated and are shown in Figures 2b and 2c. The rms misfit for this model is 14 mm; the residual interferograms exhibit random spatially-correlated errors that are different in each independent interferogram, and probably result primarily from changes in tropospheric water vapour concentrations.

3.2. Distributed-Slip Model

[10] To make the model more realistic, and to improve the fit to the data, we solved for a distributed-slip model. We chose a 60 km long fault plane (Figure 2) that follows the trace of the Denali Fault, and extends vertically to a depth of 24 km. The fault was divided into 90 patches, each 4 by 4 km. To determine the earthquake slip model, vector **m**, we used a standard linear least-squares inversion to solve the equation

$$\begin{pmatrix} \mathbf{A} \\ \gamma^2\nabla^2 \end{pmatrix}(\mathbf{m}) = \begin{pmatrix} \mathbf{d} \\ 0 \end{pmatrix} \quad (1)$$

where **A** is a matrix containing Green's functions (line of sight displacements calculated for 1 m of slip on each fault

[1] Auxiliary material is available at ftp://ftp.agu.org/apend/gl/2003GL018014.

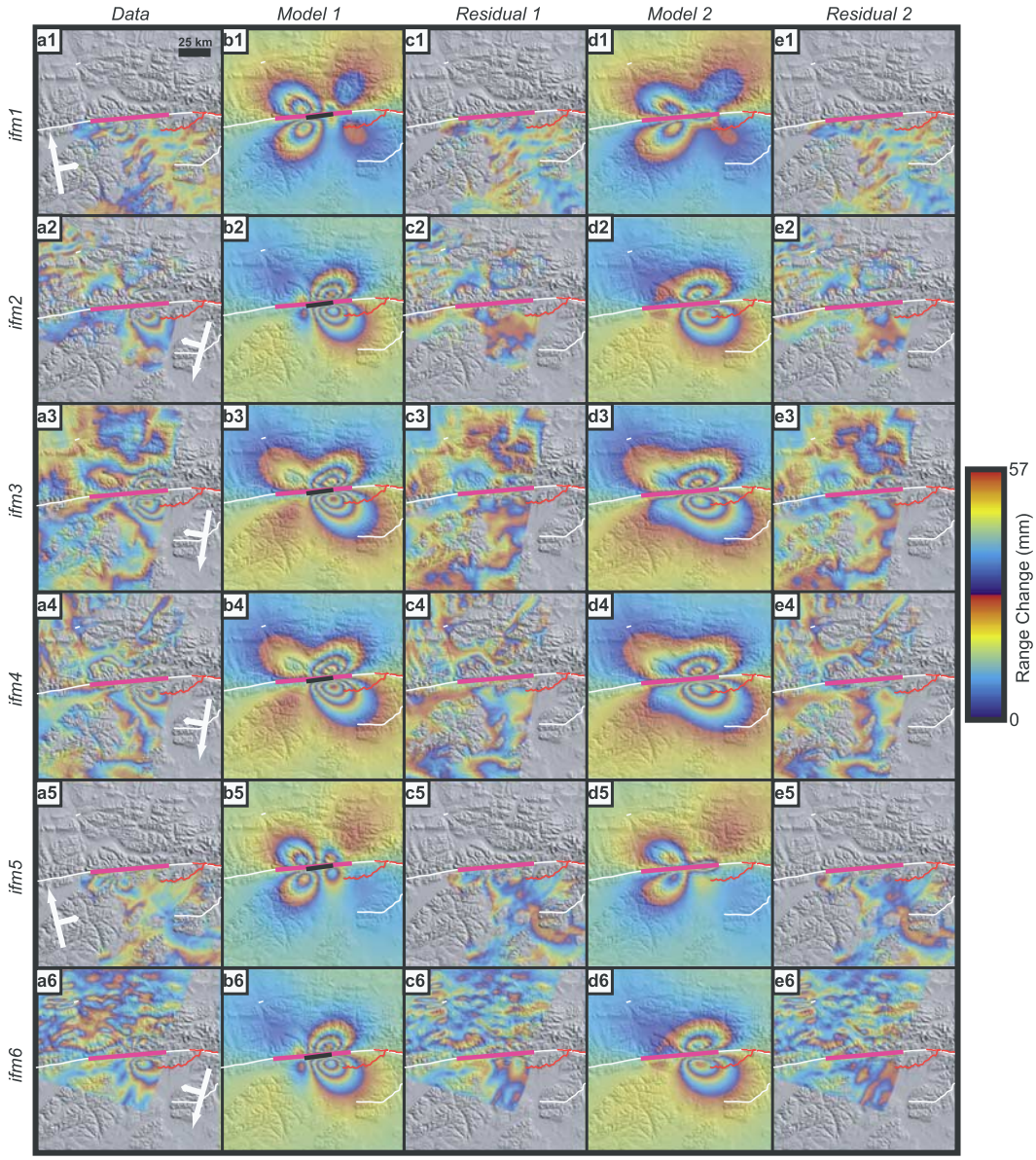

Figure 2. (a1–6) Observed interferograms for the Nenana Mountain earthquake (Table 1); (b1–6) simulated interferograms, constructed using the best-fit, single-fault model (Table 2); (c1–6) residual interferograms for single-fault model; (d1–6; e1–6) simulated interferograms and residuals for distributed slip model (Figure 3). [Black line – projected surface rupture of the single-dislocation model; thick magenta line – distributed-slip model fault plane; thin red line – surface rupture of the 3 November earthquake; white lines – other mapped faults; white arrows – satellite azimuth and look direction.]

patch using the elastic dislocation formulation of [*Okada*, 1985] and projected into the satellite line of sight); ∇^2 is the finite difference approximation of the Laplacian operator, which acts as a smoothing operator, the importance of which is governed by the size of the scalar smoothing factor γ^2, and **d** is a vector containing the observed line-of-sight displacements. We solved for both dip-slip and strike-slip components.

[11] The best-fit slip distribution depends on the size of the smoothing factor γ^2: high values lead to an over-smooth solution with large misfit, low values result in smaller misfits, but oscillating slip distributions. To find the appropriate value for γ^2, we plot solution roughness (defined as the mean absolute Laplacian of the slip model) against misfit (Auxiliary Figure 2[1]). We find no benefit in having

Table 2. Source Parameters From InSAR and Seismology

	InSAR[a]	Harvard CMT	K&Y[b]
Strike	261.8 ± 0.9°	262°	265°
Dip	81.2 ± 1.7°	89°	80°
Rake	173.7 ± 1.3°	179°	179°
Slip (m)	1 (fixed)	—	1.4
Length (km)	21.5 ± 1.0	—	30
Depth[c](km)	12.9 ± 0.7	15.8	10
Width (km)	15.4 ± 1.3	—	10
Longitude	−148.047 ± 0.004°	−148.13°	−148.04°
Latitude	63.478 ± 0.002°	63.58°	63.62°
M_0[d](10^{18}Nm)	10.8 ± 0.8	10.9	12
M_w	6.66 ± 0.02	6.66	6.69

[a]Best-fit single dislocation model.
[b]*Kikuchi andYamanaha* [2002].
[c]Centroid Depth.
[d]Assuming Lamé parameters $\lambda = \mu = 32.3$ GPa.

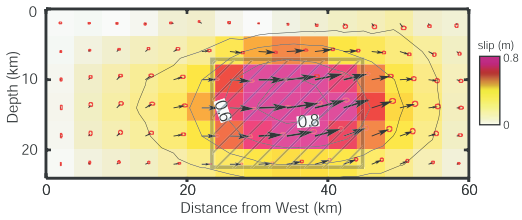

Figure 3. Distributed slip model for the Nenana mountain earthquake. Colors and contours show magnitude of slip; arrows show relative motion of north side of fault with respect to the south, with 95% confidence limits shown as red ellipses. The grey box delimits the area where 1 m slip was found for the uniform slip model. The model fault plane location is shown as a thick magenta line in Figure 2.

slip models with roughness greater than 2 mm/km; solutions smoother than this fit the data poorly.

[12] The resultant slip model shows a simple, elliptical pattern of slip, reaching a maximum of 890 ± 30 mm at a depth of 12–16 km (Figure 3). The maximum average slip for the top 4 km is just 160 ± 30 mm. While predominantly strike slip, the model has a dip slip component (north side up) of up to 230 ± 20 mm in the eastern half of the rupture. The rms residual (12 mm) is smaller than that of the single fault model, although the improvement is marginal (Figures 2d and 2e). The model has a moment of 13.5 ± 0.5 × 10^{18} Nm (M_w = 6.72 ± 0.01). Slip errors were again determined using Monte Carlo simulation, and were found to be less than ~40 mm for most of the model, although the errors are larger for inversions with less smoothing. We repeated the inversion using a fault that dipped north at 81°, as suggested by the single-fault inversion solution. The slip distribution and misfit was virtually indistinguishable from the vertical-fault model.

[13] Inversion of synthetic interferograms with the same data distribution, generated using a checkerboard slip pattern with added noise, have large misfits for solutions with roughness less than ~6 mm/km – a rougher model than the real data require. We are able to recover the checkerboard slip distribution well in the upper ~10 km (Auxiliary Figure 3[1]), indicating we have good resolution there.

4. Conclusions

[14] The Nenana Mountain Earthquake appears to have been a fairly simple event, with up to 0.9 m of slip occurring along the Denali Fault at depth. The InSAR data confirm that there was no significant surface rupture for the earthquake, and that slip in the upper 4 km of crust was small.

[15] InSAR is the most accurate method for determining the location of earthquakes in remote areas, and our model therefore enables stress-triggering calculations to be refined. We repeated the calculations of *Anderson and Ji* [2003] to determine the static Coulomb stress transferred from the Nenana Mountain Earthquake to the hypocentral area of the 3 November 2002, Denali Earthquake (Auxiliary Figure 4[1]). The earthquake initiated with thrusting on the Susitna Glacier Fault, whose geometry we determined from InSAR [*Lu et al.*, 2003]. The Nenana Mountain Earthquake increased the Coulomb stress at the Denali Earthquake hypocenter by 30–60 kPa (Auxiliary Figure 4[1]), encouraging the subsequent failure.

[17] **Acknowledgments.** TJW is supported by a NERC postdoctoral research fellowship. Radarsat-1 and ERS-2 SAR images are © 2002 Canadian Space Agency and European Space Agency, respectively, and were provided by the Alaska SAR Facility (ASF). Part of this research was performed at the SAIC, EROS Data Center under USGS contract O3CRCN0001 and funding from NASA (NRA-99-OES-10 RADARSAT-0025-0056). We thank J. Hales, V. Wolf, and other ASF staff members for their special efforts in making the SAR data available to us; Greg Anderson and Emre Evren for assistance with stress change calculations; Peter Haussler and Kerry Sieh for discussing their field observations, and Jim Savage and two anonymous reviewers whose comments improved the manuscript. Some figures were prepared using the public domain Generic Mapping Tools GMT [*Wessel and Smith*, 1998].

References

Anderson, G., and C. Ji, Static stress transfer during the 2002 Nenana Mountain-Denali Fault, Alaska, earthquake sequence, *Geophys. Res. Lett.*, *30*(6), 1310, doi:10.1029/2002GL016724, 2003.

Eberhart-Phillips, D., et al., The 2002 Denali fault earthquake, Alaska: A large magnitude, slip-partitioned event, *Science*, *300*, 1113–1118, 2003.

Goldstein, R. M., and C. L. Werner, Radar interferogram filtering for geophysical applications, *Geophys. Res. Lett.*, *25*, 4035–4038, 1998.

Hanssen, R., *Radar interferometry: Data interpretation and error analysis*, Kluwer Acad., Netherlands, 2001.

Jónsson, S., H. Zebker, P. Segall, and F. Amelung, Fault slip distribution of the 1999 Mw 7.1 Hector Mine earthquake, California, estimated from satellite radar and GPS measurements, *Bull. Seismol. Soc. Am.*, *92*, 1377–1389, 2002.

Kikuchi, M., and Y. Yamanaka, Source rupture processes of the central Alaska earthquake of Nov. 3, 2002, inferred from teleseismic body waves (+ the 10/23 M6.7 event), *EIC Seismological Note, 129*, 2002.

Lu, Z., T. J. Wright, and C. Wicks, Deformation of the 2002 Denali Fault earthquakes, Alaska, mapped by Radarsat-1 interferometry, *Eos Trans. AGU*, in press, 2003.

Massonnet, D., and K. L. Feigl, Radar interferometry and its application to changes in the earth's surface, *Rev. Geophys.*, *36*(4), 441–500, 1998.

Okada, Y., Surface deformation due to shear and tensile faults in a half-space, *Bull. Seismol. Soc. Am.*, *75*, 1135–1154, 1985.

Pegler, G., and S. Das, Analysis of the relationship between seismic moment and fault length for large crustal strike-slip earthquakes between 1977–92, *Geophys. Res. Lett.*, *23*(9), 905–908, 1996.

Wessel, P., and W. H. F. Smith, New, improved version of generic mapping tools released, *EOS Trans. Amer. Geophys. U.*, *79*(47), 579, 1998.

Wright, T. J., Remote monitoring of the earthquake cycle using satellite radar interferometry, *Phil. Trans. R. Soc. Lond. A*, *360*, 2873–2888, 2002.

Wright, T. J., B. Parsons, J. Jackson, M. Haynes, E. Fielding, P. England, and P. Clarke, Source parameters of the 1 October 1995 Dinar (Turkey) earthquake from SAR interferometry and seismic bodywave modelling, *Earth Planet. Sci. Lett.*, *172*, 23–37, 1999.

T. J. Wright, Centre for the Observation and Modelling of Earthquakes and Tectonics, Department of Earth Sciences, Parks Road, Oxford, OX1 3PR, UK. (tim.wright@earth.ox.ac.uk)

Z. Lu, U.S. Geological Survey, EROS Data Center, SAIC, 47914 252nd St., Sioux Falls, SD 57196, USA. (lu@usgs.gov)

C. Wicks, U.S. Geological Survey, Earthquake Hazards Program, 345 Middlefield Road, MS-977, Menlo Park, CA 94025, USA. (cwicks@usgs.gov)